An efficient discontinuous Galerkin method for aeroacoustic propagation

An efficient discontinuous Galerkin method for aeroacoustic propagation

R. Della Ratta Rinaldi, A. Iob and R. Arina*,†

Dipartimento di Ingegneria Aeronautica e Spaziale - Politecnico di Torino, 10129 Torino, Italy

1. INTRODUCTION

Numerical simulation of the acoustic radiation associated to fluid flow requires highly accurate and efficient algorithms able to mimic the nondispersive and nondiffusive nature of the acoustic waves propagating over long distances. One of the most popular numerical scheme in computational aeroacoustics (CAA) is the dispersion relation preserving algorithm originally proposed by Tam and Webb [1]. It is designed for Cartesian or highly regular curvilinear coordinates. However, in many practical applications, complex geometries must be considered and unstructured grids may be necessary. One of the most promising numerical schemes able to fulfill all the above requirements is the discontinuous Galerkin method (DGM).

The DGM was first proposed in the early 1970s by Reed and Hill in the frame of the neutron transport [2]. Since then, the method has found its use in many different computational models. More recently, in the context of CFD, DGM has gained an increasing popularity because of its superior properties with respect to more traditional schemes in terms of accuracy and intrinsic stability for convection [3]. An exhaustive survey of the most important applications of the DGM for convection-dominated problems can be found in the book of Cockburn *et al*. [4].

Nevertheless, it is in the context of the wave propagation phenomena in complex geometries, governed by the Maxwell equations or the linearized Euler equations, that the DGM has proved its superiority the most. The increasing number of papers published on the subject indicates that the development of efficient DGMs is an active research topic. Many studies deal with the DGM accuracy properties, such as dissipation and dispersive properties. Hu and Atkins analyzed the DGM

*Correspondence to: R. Arina, DIASP - Politecnico di Torino, Corso Duca degli Abruzzi 24, 10129 Torino, Italy.
†E-mail: renzo.arina@polito.it

in one dimension on nonuniform grids for wave propagation using the linearized Euler equations [5]. They found superaccuracy in wavenumber space of $2p + 2$, which is twice the order of accuracy of the basis functions of degree p. They also showed similar results for unstructured grids in two dimensions [6]. Later, Ainsworth proved the conjectures of Hu and Atkins about the dispersion and dissipation properties of the DGM in one dimension [7]. Similar analysis can be found in [8]. Examples of applications of the DGM for the solution of aeroacoustic problems are reported, among others, in [9].

The DGM displays many interesting properties. It is compact: regardless of the order of the element, data are only exchanged between neighboring elements. It is well suited for complex geometries because it can be applied to an unstructured grid, even nonconformal. The expected dispersion and dissipation properties are retained also on unstructured grids. Another advantage of the DGM is the straightforward implementation of boundary conditions, because only the flux needs to be specified at the boundary. One of the disadvantages of the DGM is its computational cost. Because of the discontinuous character, there are extra DOFs at cell boundaries in comparison to the continuous finite elements, demanding more computational resources. This drawback can be partially reduced with a parallel implementation of the algorithm, an operation that is not too difficult because of the compactness property of the scheme [10, 11].

Another disadvantage of the original formulation is the need for quadrature for the weighted residual formulation, but it can be eliminated by adopting the quadrature-free approach proposed by Atkins and Shu [12]. Considering only elements with constant Jacobian, that is, with a linear mapping to the reference element, all integrals can be evaluated during the initialization step. Because of the assumption of linear reference-element mapping, with the quadrature-free approach only triangles and quadrangles with straight edges can be used.

In the present work, the DGM is applied to the solution of the linearized Euler equations (LEEs) and of the acoustic perturbation equations (APE) [13], for the numerical simulation of aeroacoustic propagation in two-dimensional and axisymmetric geometries, with triangular and quadrilateral elements. To improve computational efficiency, it is possible to adopt a variable interpolation order strategy, as proposed by Chevaugeon *et al.* [14]. Here, a novel approach based on local error estimation is proposed. The element degree is relaxed near geometrical singularities. In this way a strong reduction in computational time is achieved, still keeping an accurate solution with respect to the constant order case. In addition, the DGM is implemented with the quadrature-free approach. The time discretization is based on a low dissipation formulation of a fourth-order accurate Runge–Kutta scheme [15]. Explicit time integration, the more appropriate for acoustic wave propagation, avoids inversion of a large algebraic system, and it is well suited for parallel computation. Along the far-field boundaries, to avoid incoming spurious reflections, a perfectly matched layer (PML) boundary condition is used [16]. The LEE or APE governs acoustic wave propagation in regions where the mean flow is nonuniform. However, in the far-field the mean flow field is essentially uniform. Therefore, to reduce the computational effort, it is possible to switch to a less computationally demanding mathematical model. This is done by coupling the DGM with the three-dimensional integral formulation of the wave equation proposed by Ffowcs Williams and Hawkings (FW-H) [17] to evaluate directivity patterns at very long distances.

The DGM formulation and the time integration scheme are presented in Sections 2 and 3 respectively. The application of the proposed DGM to the numerical solution of the LEE is presented in Section 4, and of the APE in Section 5. The properties of the DGM, including the new variable element degree formulation, are presented in Section 6. The coupling with the Ffowcs Williams and Hawkings formulation is described in Section 7. Calculations of test cases are discussed in Section 8 and conclusions are drawn in Section 9.

2. QUADRATURE FREE DISCONTINUOUS GALERKIN METHOD

Considering a hyperbolic conservation equation of the form

$$\frac{\partial \boldsymbol{u}}{\partial t} + \nabla \cdot \boldsymbol{F}(\boldsymbol{u}) = 0\,, \tag{1}$$

where $\boldsymbol{u}$ is a vector of dimension N_{var} and $\boldsymbol{F}(\boldsymbol{u})$ is the flux vector. Partitioning the domain into nonoverlapping elements Γ_i, where i is the element index, the DGM can be obtained applying a traditional Galerkin projection method to each element. Inside each element, the solution is approximated by a linear combination of basis functions

$$\boldsymbol{u}_{\Gamma_i} \equiv \boldsymbol{v}_i \approx \sum_{l=1}^{N} v_{i,l}\, b_l \,, \tag{2}$$

where $\boldsymbol{v}$ is the test function, b_l is the l-th basis and N is the number of DOFs on each element. Here, according to the semidiscrete approach, the basis set contains only spatial functions and the solution expansion coefficients $v_{i,l}$ are a function of time only. Then, using expansion (2) and projecting the governing Equation (1) onto each member of the basis set, the weak form of the problem can be written, for the Γ_i element, as

$$\int_{\Gamma_i} b_k \left(\frac{\partial \boldsymbol{v}}{\partial t} + \nabla \cdot \boldsymbol{F} \right)_i \mathrm{d}\Gamma = \int_{\Gamma_i} b_k \quad \sum_{l=1}^{N} \frac{\mathrm{d}v_l}{\mathrm{d}t}\, b_l + \nabla \cdot \boldsymbol{F} \Bigg)_i \mathrm{d}\Gamma = 0 \,, \tag{3}$$

with $1 \leqslant k \leqslant N$, $1 \leqslant i \leqslant I$, and I being the total number of elements. To obtain an expression that explicitly contains the flux at the element interfaces, the divergence term in Equation (3) is integrated by parts

$$\int_{\Gamma_i} b_k \quad \sum_{l=1}^{N} \frac{\mathrm{d}v_{i,l}}{\mathrm{d}t} b_l \Bigg) \mathrm{d}\Gamma + \int_{\partial\Gamma_i} b_k \boldsymbol{F}_i \cdot \boldsymbol{n} \mathrm{d}\sigma - \int_{\Gamma_i} \nabla b_k \boldsymbol{F}_i \mathrm{d}\Gamma = 0 \,, \tag{4}$$

where $\boldsymbol{n}$ is the outward-pointing normal versor referred to each element edge. Flux vectors $\boldsymbol{F}_i$ are approximated in terms of the basis set as [12]

$$\boldsymbol{F}_i = \sum_{l=1}^{N} \boldsymbol{f}_{i,l}\, b_l \,; \qquad \boldsymbol{F}_i \cdot \boldsymbol{n} = \sum_{l=1}^{N_{\text{edge}}} (\boldsymbol{f}_i \cdot \boldsymbol{n})_l\, \bar{b}_l \,, \tag{5}$$

where $\boldsymbol{f}_{i,l}$ are the flux expansion coefficients, $\bar{b}_l$ is the edge basis set and N_{edge} is the number of DOFs on the element edge. Using expressions (5), the final form of the weak formulation can be written as

$$\int_{\Gamma_i} b_k \quad \sum_{l=1}^{N} \frac{\mathrm{d}v_{i,l}}{\mathrm{d}t} b_l \Bigg) \mathrm{d}\Gamma + \int_{\partial\Gamma_i} b_k \left(\sum_{l=1}^{N_{\text{edge}}} \boldsymbol{f}_i \cdot \boldsymbol{n} \right)_l \bar{b}_l \,\mathrm{d}\sigma - \int_{\Gamma_i} \nabla b_k \quad \sum_{l=1}^{N} \boldsymbol{f}_{i,l} b_l \Bigg) \mathrm{d}\Gamma = 0 \,, \tag{6}$$

with $k = 1, \ldots, N$. In principle the integrals of Equation (6) should be evaluated for every element of the mesh. However, it is convenient to map every element to a reference one, $\hat{\Omega}$, and to perform integrations only on this master element defined in the (ξ, η)-coordinate system. For triangular elements, the reference element $\hat{\Omega}_T$ is the unit right triangle with vertices $(\xi_1, \eta_1) = (0, 0)$, $(\xi_2, \eta_2) = (1, 0)$, and $(\xi_3, \eta_3) = (0, 1)$. For quadrangles the master element is the square centered in $(\xi, \eta) = (0, 0)$ with a side length $l_{\text{side}} = 2$. If the mapping to the reference element is linear, the Jacobian of the transformation $\boldsymbol{J}$ is constant and therefore it can be taken out of the integrals. In this way the functions to be integrated are independent of the specific element and can be evaluated analytically at the initialization step. This approach is called quadrature-free [12] because no numerical integration has to be performed during the time integration. Only triangles and rectangles with straight edges will be used in the discretization to adopt the quadrature-free formulation. The integrals of Equation (6) can be evaluated on the reference elements and grouped to form the mass

matrix $\boldsymbol{M}$ of size $N \times N$, the matrix $\boldsymbol{B}_{\text{edge}}$ of size $N \times N_{\text{edge}}$, and the stiffness tensor $\overrightarrow{\boldsymbol{K}}$ of size $N \times N \times N_{var}$,

$$\begin{aligned}
\int_{\Gamma_i} b_k b_l \mathrm{d}\Gamma &= \int_{\hat{\Omega}} b_k b_l \, \|J_i\| \, \mathrm{d}\Omega = \boldsymbol{M} \, \|J_i\| \, , \\
\int_{\Gamma_i} \nabla b_k b_l \mathrm{d}\Gamma &= \int_{\hat{\Omega}} \nabla b_k b_l \, \boldsymbol{J}^{-1} \, \|J_i\| \, \mathrm{d}\Omega = \|J_i\| \, \overrightarrow{\boldsymbol{K}} \, \boldsymbol{J}^{-1} \, , \\
\int_{\partial\Gamma_i{}^{\text{edge}}} b_k \bar{b_l} \mathrm{d}\sigma &= \int_{\partial\hat{\Omega}^{\text{edge}}} b_k \bar{b_l} \, \|\partial J_l\| \, \mathrm{d}\Sigma = \|\partial J_l\| \, \boldsymbol{B}_{\text{edge}} \, .
\end{aligned} \tag{7}$$

The bases $\{b_l\}$ are also evaluated over the master elements: they are the Lagrangian polynomials defined on the node set $T_p = \{\boldsymbol{x}_l;\, l = 1, \ldots, N\}$, where N is the number of nodes in the node set. For rectangular elements, the bases are obtained as the tensor product of the corresponding one-dimensional Lagrangian polynomials defined on the Gauss–Lobatto nodes. Given the one-dimensional polynomials $\phi_l(\xi)$ with $l = 1, \ldots, N_\xi$ and $\phi_r(\eta)$ with $r = 1, \ldots, N_\eta$, the two-dimensional ones are defined as

$$\Phi_i(\xi, \eta) = \phi_l(\xi) \cdot \phi_r(\eta) \, , \qquad i = 1, \ldots, N_\xi N_\eta \, . \tag{8}$$

For triangular elements, the Lagrangian polynomials are constructed on a set of nodes, which is defined in such a way that the internal-node positions are the solutions of a steady state, minimum energy electrostatics problem, whereas the nodes along the edges are specified as one-dimensional Gauss–Lobatto quadrature points [18].

2.1. Extension to axisymmetric problems

For axisymmetric problems, rewriting the governing equations in a cylindrical coordinate system defined as

$$r = \sqrt{x^2 + y^2} \, , \quad \theta = \arctan\left(\frac{y}{x}\right) \, , \quad z = z \, , \tag{9}$$

the DGM in cylindrical coordinates is obtained by evaluating the integrals as

$$\int_\Gamma g \, \mathrm{d}\Gamma \, = \int_\Gamma g r \, \mathrm{d}r\mathrm{d}z \, . \tag{10}$$

Expanding the functions gr of each integral of Equation (4) in terms of the basis set, that is

$$\boldsymbol{v}_i r_i \approx \sum_{l=1}^{N} (v_i r_i)_l \; b_l \, , \quad \boldsymbol{F}_i r_i = \sum_{l=1}^{N} (\boldsymbol{f}_i r_i)_l \; b_l \, , \quad \boldsymbol{F}_i \cdot \boldsymbol{n} \, r_i = \sum_{l=1}^{N_{\text{edge}}} (\boldsymbol{f}_i \cdot \boldsymbol{n} \, r_i)_l \, \bar{b}_l \, , \tag{11}$$

the final form of the weak formulation in axisymmetric coordinates can be written as

$$\int_{\Gamma_i} b_k \left[\sum_{l=1}^{N} \frac{\mathrm{d}\,(v_i r_i)_l}{\mathrm{d}t} b_l \right] \mathrm{d}\Gamma + \int_{\partial\Gamma_i} b_k \left[\sum_{l=1}^{N_{\text{edge}}} (\boldsymbol{f}_i \cdot \boldsymbol{n} \, r_i)_l \, \bar{b}_l \right] \mathrm{d}\sigma - \int_{\Gamma_i} \nabla b_k \left[\sum_{l=1}^{N} (\boldsymbol{f}_i r_i)_l \, b_l \right] \mathrm{d}\Gamma = 0. \tag{12}$$

Using the quadrature-free approach, the integrals of Equation (12) can be evaluated on the reference elements and grouped to form the matrices, similarly to the two-dimensional formulation (7).

2.2. Interface flux

Because of the discontinuous function approximation, flux terms are not uniquely defined at element interfaces. Therefore, to evaluate the flux at element interfaces, a technique traditionally used in finite volume schemes is borrowed by the discontinuous finite element formulation.

After the values of the numerical solution $\boldsymbol{V}_i$ have been computed on every element, the flux through an interface can be computed regardless of the type of elements or the orientation of the coordinate system of the elements bordering the interface. The flux function $\boldsymbol{F}(\boldsymbol{u}) \cdot \boldsymbol{n}$ appearing in Equation (4) is replaced by a numerical flux function $\boldsymbol{F}^{\mathrm{R}}(\boldsymbol{u}_l, \boldsymbol{u}_r)$, which depends on the internal interface state, on the neighboring element interface state, and on the direction $\boldsymbol{n}$ normal to the interface. At the interface, one element is arbitrarily designated to be on the left, l, and the other to be on the right, r. To guarantee the formal consistency of the scheme, $\boldsymbol{F}^{\mathrm{R}}$ is required to satisfy the relations

$$\boldsymbol{F}^{\mathrm{R}}(\boldsymbol{u}_l, \boldsymbol{u}_r) = \boldsymbol{F}(\boldsymbol{u}) \cdot \boldsymbol{n}\,, \quad \boldsymbol{F}^{\mathrm{R}}(\boldsymbol{u}_l, \boldsymbol{u}_r) = -\boldsymbol{F}^{\mathrm{R}}(\boldsymbol{u}_r, \boldsymbol{u}_l)\,, \tag{13}$$

which are the consistency and the conservative conditions respectively. In the present work, the Riemann flux $\boldsymbol{F}^{\mathrm{R}}$ is approximated by the local Lax–Friedrichs flux of the form

$$\boldsymbol{F}^{\mathrm{R}}(\boldsymbol{u}_l, \boldsymbol{u}_r) = \frac{1}{2}\left[\boldsymbol{F}(\boldsymbol{u}_l) + \boldsymbol{F}(\boldsymbol{u}_r) - \vartheta \|a\|_{\max}(\boldsymbol{u}_l - \boldsymbol{u}_r)\right], \quad \vartheta \geqslant 0\,, \tag{14}$$

where $\|a\|_{\max}$ is the maximum (absolute value) of the eigenvalues of the Jacobian matrix associated to the normal flux $\boldsymbol{F}(\boldsymbol{u}) \cdot \boldsymbol{n}$ and ϑ is an upwind parameter. The numerical solution of the weak formulation may correspond to either a physical mode or a spurious mode depending on the value of ϑ, as demonstrated by Ainsworth [7].

The local Lax–Friedrichs formula, with $\vartheta = 1$, one of the simplest Riemann flux formulations, is commonly used in many DGM implementations because of its low operational cost [12]. In this case the spurious mode is damped so quickly that it seldom has an influence in practical simulations.

3. TIME INTEGRATION

Time integration is performed using a fourth-order, six-stage Runge–Kutta scheme that has low dispersion and dissipation errors [15].

Classical third-order and fourth-order Runge–Kutta schemes provide relatively large stability limits [19] but, for acoustic calculations, the stability consideration alone is not sufficient, because the Runge–Kutta schemes retain both dissipation and dispersion errors. Hu *et al.* [20] have shown that to get time-accurate solutions in wave propagation problems, time steps much smaller than those allowed by the stability limit of the classical Runge-Kutta schemes must be used. This constraint certainly undermines the efficiency of the classical integration schemes.

Instead of choosing the coefficients of the Runge–Kutta scheme to optimize the maximum order of accuracy, it is possible to select coefficients to minimize the dissipation and the dispersion errors. Moreover, this optimization does not introduce additional stability constraints and sufficiently large time steps can be used, which therefore increase the efficiency of the computation.

The Runge–Kutta scheme is implemented using the low-storage Willamson's formulation, which only requires two storage locations per variable [21]. The low storage requirement is important for computational acoustic applications where a large memory use is expected.

4. LINEARIZED EULER EQUATIONS

The propagation of sound waves in a medium with nonuniform mean velocity $\mathbf{U}_0$, neglecting fluid viscosity and heat conduction, is governed by the LEE [22]. Depending on the case under consideration, a two-dimensional or an axisymmetric formulation is used.

4.1. Two-dimensional formulation

Considering a steady two-dimensional mean flow, LEE is formulated as

$$\frac{\partial \boldsymbol{u}}{\partial t} + \frac{\partial \boldsymbol{F}_x}{\partial x} + \frac{\partial \boldsymbol{F}_y}{\partial y} + \boldsymbol{G} = \boldsymbol{S}\,, \tag{15}$$

where $\boldsymbol{u} = [\rho', u', v', p']^T$ is the unknown vector and the superscript $(.)'$ denotes the acoustic fluctuations. ρ' and p' are the density and pressure fluctuations, respectively, and (u', v') are the components of the velocity fluctuations in (x, y) directions. $\boldsymbol{F}_x$ and $\boldsymbol{F}_y$ are the fluxes along x and y directions, respectively, $\boldsymbol{G}$ contains the mean flow derivatives and $\boldsymbol{S}$ represents the acoustic sources. The fluxes, $\boldsymbol{F}_x$ and $\boldsymbol{F}_y$, and the term $\boldsymbol{G}$ have the following expressions:

$$\boldsymbol{F}_x = \begin{pmatrix} \rho' u_0 + \rho_0 u' \\ u_0 \rho_0 u' + p' \\ u_0 \rho_0 v' \\ u_0 p' + \gamma p_0 u' \end{pmatrix}, \qquad \boldsymbol{F}_y = \begin{pmatrix} \rho' v_0 + \rho_0 v' \\ v_0 \rho_0 u' \\ v_0 \rho_0 v' + p' \\ v_0 p' + \gamma p_0 v' \end{pmatrix},$$

$$\boldsymbol{G} = \begin{pmatrix} 0 \\ (\rho_0 u' + \rho' u_0)\frac{\partial u_0}{\partial x} + (\rho_0 v' + \rho' v_0)\frac{\partial u_0}{\partial y} \\ (\rho_0 u' + \rho' u_0)\frac{\partial v_0}{\partial x} + (\rho_0 v' + \rho' v_0)\frac{\partial v_0}{\partial y} \\ (\gamma - 1)\left(p' \nabla \cdot \boldsymbol{u}_0 - u' \frac{\partial p_0}{\partial x} - v' \frac{\partial p_0}{\partial y}\right) \end{pmatrix}. \tag{16}$$

In the above expressions subscript $(.)_0$ denotes mean flow quantities and γ is the specific heat ratio of air in standard conditions. It is evident from Equation (16) that, in order to solve the LEE, the mean flow field must be known in advance.

4.2. Axisymmetric formulation

Considering axisymmetric geometries, the LEE can be written in cylindrical coordinates as

$$\frac{\partial \boldsymbol{u}}{\partial t} + \frac{\partial \boldsymbol{F}_z}{\partial z} + \frac{\partial \boldsymbol{F}_r}{\partial r} + \boldsymbol{G}_{\text{axy}} + \boldsymbol{G} = \boldsymbol{S}\,, \tag{17}$$

where $\boldsymbol{u} = [\rho', u,' v', w', p']^T$ is the acoustic perturbation vector. Here, $(u,' v', w')$ are the velocity components in (z, r, θ) direction, respectively. $\boldsymbol{F}_z$ and $\boldsymbol{F}_r$ are the fluxes along z and r directions respectively, $\boldsymbol{G}_{\text{axy}}$ contains terms of the mean flow because of axisymmetry, $\boldsymbol{G}$ contains the mean flow derivatives and $\boldsymbol{S}$ represents the acoustic sources. Assuming that the azimuthal component of the mean flow velocity is zero, $w_0 = 0$, the fluxes, $\boldsymbol{F}_z$ and $\boldsymbol{F}_r$, the terms $\boldsymbol{G}_{\text{axy}}$ and $\boldsymbol{G}$ have the following expressions:

$$\boldsymbol{F}_z = \begin{pmatrix} \rho' u_0 + \rho_0 u' \\ u_0 \rho_0 u' + p' \\ u_0 \rho_0 v' \\ u_0 \rho_0 w' \\ u_0 p' + \gamma p_0 u' \end{pmatrix}, \quad \boldsymbol{F}_r = \begin{pmatrix} \rho' v_0 + \rho_0 v' \\ v_0 \rho_0 u' \\ v_0 \rho_0 v' + p' \\ v_0 \rho_0 w' \\ v_0 p' + \gamma p_0 v' \end{pmatrix}, \quad \boldsymbol{G}_{\text{axy}} = \frac{1}{r}\begin{pmatrix} -\rho' v_0 \\ -u' v_0 \\ -v' v_0 - \frac{p'}{\rho_0} \\ 0 \\ (\gamma - 1)\, p' v_0 \end{pmatrix},$$

$$\boldsymbol{G} = \begin{pmatrix} 0 \\ (\rho_0 u' + \rho' u_0)\frac{\partial u_0}{\partial z} + (\rho_0 v' + \rho' v_0)\frac{\partial u_0}{\partial r} \\ (\rho_0 u' + \rho' u_0)\frac{\partial v_0}{\partial z} + (\rho_0 v' + \rho' v_0)\frac{\partial v_0}{\partial r} \\ -w'\left(\frac{\partial u_0}{\partial z} + \frac{\partial v_0}{\partial r}\right) \\ (\gamma - 1)\left[p'\left(\frac{\partial u_0}{\partial z} + \frac{\partial v_0}{\partial r}\right)\right] - u' \frac{\partial p_0}{\partial z} - v' \frac{\partial p_0}{\partial r} \end{pmatrix}. \tag{18}$$

4.3. Wall boundary conditions

Walls are assumed impermeable and acoustically rigid; this means that no flow passes through the boundary and that acoustic waves are totally reflected. The flux normal to a wall is evaluated using the relation

$$\boldsymbol{F}_n = \boldsymbol{F}_x n_x + \boldsymbol{F}_y n_y \,, \tag{19}$$

where $\boldsymbol{F}_x$ and $\boldsymbol{F}_y$ are evaluated with Equation (16) imposing wall conditions for pressure and velocity fluctuations. Assuming that the mean flow satisfies the slip flow boundary condition, an analogous slip flow condition must be imposed on the velocity fluctuations

$$\boldsymbol{u}'_w = 0 \,, \tag{20}$$

where $\boldsymbol{u}'_w = u'_w \cdot \boldsymbol{n}$ is the acoustic velocity normal to the wall and $\boldsymbol{n}$ is the normal versor.
A vector $\boldsymbol{V}$ can be modified to have zero normal component, with respect to the normal $\boldsymbol{n}$, by replacing it with a vector $\boldsymbol{W}$ defined as

$$\boldsymbol{W} = \boldsymbol{V} - (\boldsymbol{V} \cdot \boldsymbol{n})\, \boldsymbol{n} \,, \quad \text{so that} \quad \boldsymbol{W} \cdot \boldsymbol{n} = 0 \,. \tag{21}$$

Therefore, on a wall boundary, the acoustic velocity at the time $j+1$ is evaluated as

$$\left(\boldsymbol{u}'_w\right)^{j+1} = \left(\boldsymbol{u}'_w\right)^{j} - \left[\left(\boldsymbol{u}'_w\right)^{j} \cdot \boldsymbol{n}\right] \boldsymbol{n} \,. \tag{22}$$

The pressure fluctuations at the wall are evaluated linearizing the exact solution of the Riemann problem for a reflective wall [23]. This solution, in two dimensions, can be written as

$$\left(p'_w\right)^{j+1} = \left(p'_w\right)^{j} + p_0 \frac{\gamma}{c_0} \left(u'_w\right)^{j} \,, \tag{23}$$

where the mean flow velocity is assumed tangent to the wall.

To show the accuracy of the wall boundary formulation the case of a monopole near a wall is considered. The normal velocity component in a point on the wall is plotted as a function of time (Figure 1). It is evident that using Equations (22) and (23) the solution is more accurate than taking the value of the pressure from neighbor cells, as usually done in DGM.

4.4. Nonreflecting boundary conditions

One of the major issues in CAA is to truncate the far-field domain preserving a physically meaning solution. This leads to the necessity of having accurate and robust nonreflecting far-field boundary conditions. A large number of families of nonreflecting boundary conditions has been proposed in the literature. The most widely used for the Euler equations are the characteristic-based boundary

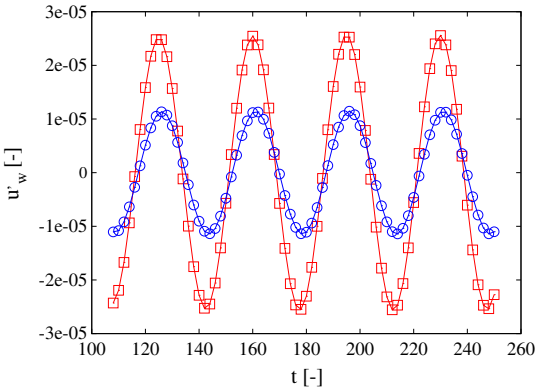

Figure 1. Normal velocity at wall as a function of time. Pressure wall boundary condition : ∘ based on linearized solution of the Riemann problem; □ value from neighbor cells.

conditions [24, 25]. These methods are derived applying the one-dimensional characteristic variable splitting along the boundary normal direction. These techniques have proved to be efficient and robust. The main drawback is that reflections are prevented only for waves that are traveling in the boundary-normal direction. Non-negligible reflections can be seen for waves impinging the boundary with other angles.

Another family of nonreflective boundary conditions is composed by the buffer zone technique [26]. In this case, an extra zone is added to damp the reflected waves. The damping can be introduced as a low-pass filter, grid stretching or accelerating the mean flow to supersonic speeds. The main drawback of these techniques is represented by the increase of the computational cost, because the thickness of the buffer zone could be important to achieve a good level of accuracy.

Recently, the PML technique has been developed as a new class of nonreflective boundary conditions. The basic idea of the PML approach is to modify the governing equations to absorb the outgoing waves in the layer. The advantage of this technique is that the absorbing layer is theoretically capable of damping waves independently from the impinging direction and frequency, employing thinner layers with respect to the other buffer zone approaches, with benefits on the efficiency and the accuracy of the solution.

The PML technique was extended to CAA applying the split physical-variable formulation to the LEE with uniform mean flow [27]. It was shown that the PML absorbing zone is theoretically reflectionless to the acoustic, vorticity and entropy waves. Nonetheless, a numerical instability arises in this formulation, and the presence of instability waves has been analyzed by Tam *et al.* [28]. It was shown [29] that the instability of the split formulation is due to an inconsistency of the phase and group velocity of the acoustic waves in the presence of a mean flow, and a stable PML for the LEE was proposed on the basis of an unsplit physical-variable formulation. This approach, which has been also extended to nonuniform mean flows [16], is employed in the present work.

The PML formulation is also used to impose incoming waves at acoustic inlet boundaries. On those boundaries incoming waves should be specified, but at the same time outgoing waves should leave the computational domain without reflections. This can be achieved by applying the PML equations to the reflected wave, $\boldsymbol{u}_{\mathrm{re}}$ [30], which can be expressed as the total acoustic field, $\boldsymbol{u}$, minus the incoming prescribed acoustic wave, $\boldsymbol{u}_{\mathrm{in}}$.

5. ACOUSTIC PERTURBATION EQUATIONS

Linearized Euler equations support hydrodynamic instability waves, such as the Kelvin–Helmholtz ones; therefore, when the mean flow is nonuniform, instabilities may occur. To overcome this problem a variant of these equations, called APEs, has been derived [13]. In contrast to the LEE, in the APE the nonacoustic modes of vorticity and entropy are neglected. Thus, they are stable for arbitrary mean flow fields, that is, no instability waves, as in the LEE, can occur. Furthermore, the source term of the APE fully controls the perturbation vorticity in the solution, that is, no vorticity can exist beyond the source regions. On the other hand, the wave operator in the left-hand side of the APE, is exact only in the case of irrotational mean flow fields; consequently, the presence of mean vorticity may cause errors in the computed sound propagation. These errors are assumed to be small for low mean vorticity levels [13]. There are several formulations for the APE; in this work the APE-4 system [13] is used. Assuming two-dimensional Cartesian coordinates and constant sound speed c_0, APEs are expressed as

$$\frac{\partial \boldsymbol{q}}{\partial t} + \frac{\partial \boldsymbol{F}_x}{\partial x} + \frac{\partial \boldsymbol{F}_y}{\partial y} = \tilde{\boldsymbol{S}} \,, \tag{24}$$

where $\boldsymbol{q} = [p', u', v']^T$, and the expressions for the fluxes are the following:

$$\boldsymbol{F}_x = \begin{pmatrix} u_0 p' + \rho_0 c_0^2 u' \\ p'/\rho_0 + u_0 u' + v_0 v' \\ 0 \end{pmatrix}, \quad \boldsymbol{F}_y = \begin{pmatrix} v_0 p' + \rho_0 c_0^2 v' \\ 0 \\ p'/\rho_0 + u_0 u' + v_0 v' \end{pmatrix}. \tag{25}$$

The boundary conditions associated with the APE are the same as used for the LEE.

DOI: 10.1002/fld

6. PROPERTIES OF THE DGM

6.1. Dispersion and dissipation errors

To test the dissipative and dispersive properties of the high-order DGM, following Ainsworth [7], a plane wave with a real wave number $k = \pi/2$ propagating along the x-axis of a duct in a medium at rest is considered. Different structured regular grids are taken into account with $1.02 \leqslant h \leqslant 4.36$, where h is the average cell size. As will be seen later, because of the local nature of the DGM, the type of the grid used has no impact on the accuracy of the solution. Because of the numerical discretization, the exact wave number k is replaced by a discrete one, identified as $\tilde{k}$. The relative error between the analytical and the numerical solutions can be defined as

$$\rho = \frac{\mathrm{e}^{\mathrm{i}hk} - \mathrm{e}^{\mathrm{i}h\tilde{k}}}{\mathrm{e}^{\mathrm{i}hk}} \approx \mathrm{i}h\left(k - \tilde{k}\right) , \tag{26}$$

The error ρ is a complex number whose real part represents the dispersive error and the imaginary part the dissipative error. It is demonstrated that as the degree of the Lagrangian basis p is increased, the dissipation and dispersion errors pass through three different phases depending on the value of kh. In the unresolved regime where $2p + 1 < kh - o(kh)^{1/3}$, the error oscillates without decay as the order is increased. At the opposite extreme, if the order is sufficiently large, $2p + 1 > kh - o(kh)^{1/3}$, then the error reduces at a super-exponential rate. In the limit of $kh << 1$, the relative error converges as

$$\begin{aligned} \textit{dispersion error} &: O(kh)^{2p+3} , \\ \textit{dissipation error} &: O(kh)^{2p+2} . \end{aligned}$$

Although most analysis of dispersive behavior are performed under the assumption that $kh << 1$, in many practical applications the value of kh is imposed by the smallest mesh size h that can be resolved by the available computational resources, rather than the highest frequency of physical interest. Therefore, the computations are often performed with $kh > 1$. In Figure 2, dissipation and dispersion errors are reported for some values of $kh = O(1)$ and $p = 4$. It can be shown that as kh decreases towards $kh << 1$ both errors converge to the predicted super-exponential rate of decay. Choosing the arbitrary criteria of having both the dispersion and dissipation errors less than $E_{\max} = 5 \cdot 10^{-4}$, the accuracy limit of the method is equal to $\lambda/h \approx 2$. This means that, for $p = 4$, two elements per wavelength are sufficient to discretize the wave with the chosen accuracy.

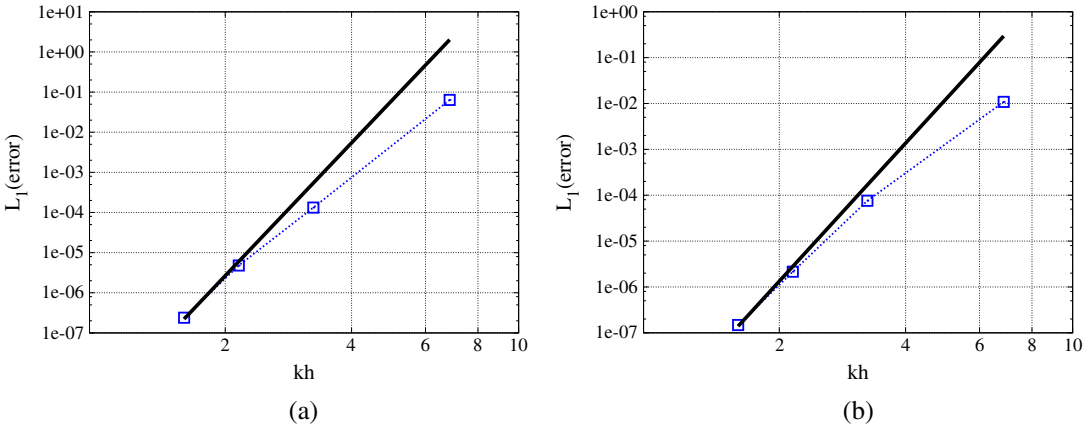

Figure 2. Dispersion (a) and dissipation (b) errors. (—) Super-exponential rate of decay, (···) numerical results, $p = 4$.

6.2. *Accuracy*

To asses the accuracy of the numerical method for different grids, the propagation of a Gaussian acoustic pulse in a medium at rest is studied. In this case the LEE and APE models coincide, being the wave propagation governed by the homogeneous wave equation. The acoustic pulse is generated at $t = 0$, at the origin of the axis as an initial disturbance of equation $p' = \epsilon_{\text{ac}} e^{-\alpha_{\text{ac}} r^2}$, with $\epsilon_{\text{ac}} = 0.01$ and $\alpha_{\text{ac}} = 0.0752$. The pressure distribution is reported in Figure 3(b)). Several computations were performed on the fixed domain $[-90, 90] \times [-90, 90]$ increasing the number of mesh elements. The results are obtained using both structured and unstructured grids (see Figure 3(a)). Being interested only in the spatial accuracy, the time step was chosen to be sufficiently small such that the error would be dominated by the spatial operator. The L_1-norm of the error for the acoustic pressure is evaluated as

$$L_1 = \frac{\sum_{i=1}^{\text{DOF}} |p_i - p_{i\,\text{exact}}|}{\text{DOF}}, \tag{27}$$

where DOF are the the degrees of freedom, that is the number of elements I times the number of nodes per element N_n. In Figure 4 the L_1-norm is plotted as a function of the square root of the

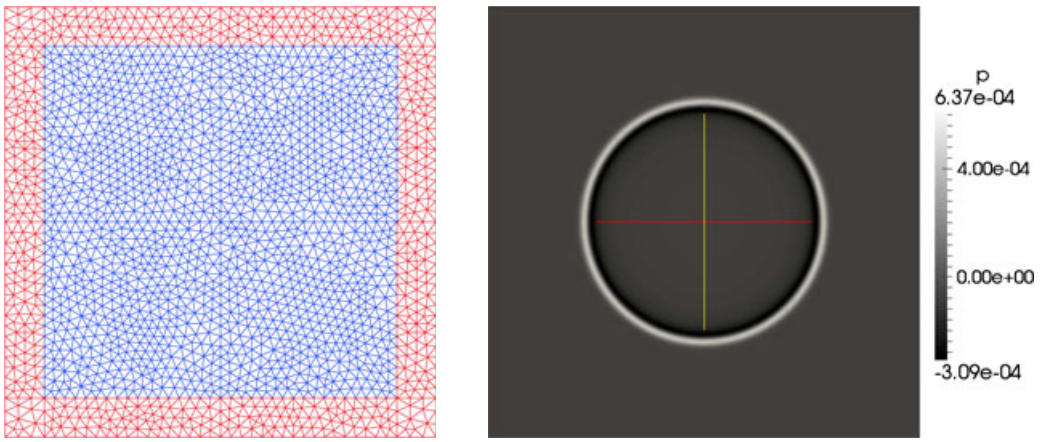

(a) (b)

Figure 3. Accuracy test case: (a) unstructured example-mesh and (b) fluctuating pressure field of a Gaussian pulse at $t = 60$.

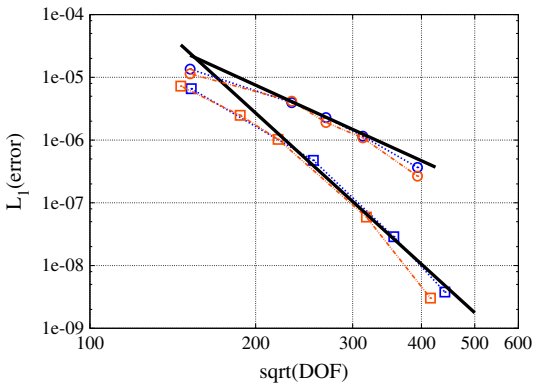

Figure 4. Accuracy for the pulse test case, using Lagrangian basis of degree $p = 3$ ($\circ$) and $p = 7$ ($\square$). ($\cdots$) Structured grids, ($- \cdot\cdot -$) unstructured grids, (—) theoretical rates of decay ($p + 1$).

DOFs, for Lagrangian basis of degree $p = 3$ and $p = 7$. One of the major motivations for employing a DGM is its ability to maintain accuracy in the case of complex geometries. The numerical tests show that in both cases, structured and unstructured grids, DGM converges at the designed rate of $p + 1$.

6.3. Variable element degree

One of the main advantages of the DGM is the compactness of the stencil allowing an easy implementation of a variable element degree algorithm. The approach is useful in the presence of very small cells, necessary for correctly resolving geometrical details. Curved boundaries can also be resolved using geometrically high-order elements. However, the generation of high-order curved meshes is not trivial and the quadrature-free approach does not apply to elements with varying Jacobian [3, 31]. On the other side, a high-order discretization with many small straight-edge elements implies extremely small time steps to satisfy the CFL stability condition. Relaxing the discretization order reduces the stability constraint, leading to a strong reduction in computational time keeping an accurate solution with respect to the constant order case.

The interface flux evaluation has to be modified when considering elements with variable degree. Because the interpolation order may vary from one element to the next, variables on interfaces have to be projected on the neighboring functional spaces. On the interface between two neighboring elements, a generic variable u can be expanded either in terms of the left-side basis set, $\left\{b_j^L\right\}$, or in terms of the right-side one $\left\{b_j^R\right\}$

$$u = \sum_{j=1}^{N} u_j^R b_j^R = \sum_{i=1}^{M} u_i^L b_i^L \,. \tag{28}$$

To project the left-side basis set onto the right-side one, the weak form of Equation (28) reads

$$\int_\Gamma b_k^R \sum_{j=1}^{N} u_j^R b_j^R \mathrm{d}\Gamma = \int_\Gamma b_k^R \sum_{i=1}^{M} u_i^L b_i^L \mathrm{d}\Gamma \,, \quad 1 \leqslant k \leqslant N \,, \tag{29}$$

where the test functions are the basis of the right side of the interface. Integrals (29) can be grouped to form mapping matrices $\boldsymbol{C}$ as

$$\boldsymbol{C^{RR}} = \int_\Gamma b_k^R b_j^R \mathrm{d}\Gamma \,, \quad \boldsymbol{C^{RL}} = \int_\Gamma b_k^R b_i^L \mathrm{d}\Gamma \,, \tag{30}$$

obtaining

$$\boldsymbol{u}^R = \left(\boldsymbol{C}^{RR}\right)^{-1} \boldsymbol{C}^{RL} \boldsymbol{u}^L \,. \tag{31}$$

Similarly, mapping R onto L leads to

$$\boldsymbol{u}^L = \left(\boldsymbol{C}^{LL}\right)^{-1} \boldsymbol{C}^{LR} \boldsymbol{u}^R \,. \tag{32}$$

The element degree is distributed according to the law suggested by Ainsworth [7]

$$2p + 1 \approx a_d h k \,, \tag{33}$$

where p is the local polynomial order, h is the local element size and k is the highest wave number of the signal to be resolved. One can choose the lowest degree to use so that the desired accuracy is achieved. The constant a_d is then calculated applying Equation (33) to the element with the smallest size. The advantages of using this approach are clearly shown in Section 8.2.

6.4. Parallelization

To parallelize the computation, the domain must be subdivided into a number of polygonal partitions. The partitioning is achieved using the open-source package METIS [32], which attempts to balance the load and minimize the communication among the processors. Once the domain has been partitioned, the computation in each partition is assigned to a separate processor. Every processor resolves its own subdomain and, during the calculation, the only communications among the processors take place when evaluating the interface fluxes. Therefore, the parallelization of the scheme is rather simple: the data that need to be exchanged are the left and right values of the field on each interface element of the partition boundary, prior to the computation of the fluxes on those interface elements. This limited intercommunication between partitions is one of the positive features of the explicit DGM, leading to an efficient parallelization. At the end of the computation the global solution is gathered on the master processor which does the output. All the communications between the partitions were implemented using the Message-Passage-Interface (MPI) (University of Tennessee, Knoxville, Tennessee) interface.

The parallel performance of the present method is shown in Figure 5, where the speed up is plotted versus the number of processors. The numerical curve follows an interpolation line of slope 0.97, which is very close to the theoretical linear scaling. The results of Figure 5 are obtained solving the acoustic pulse test case presented in Section 6.2, with a structured grid of approximately $22,000$ triangular elements and Lagrangian basis of degree $p = 7$, that is, with approximately $800,000$ nodes. At the boundaries, wall condition is imposed. The scalability calculations were performed on the cluster of Hepia, Genève, composed of 14 twin boards, each with a double CPU quad core Intel Xeon E5530 (©Intel Corporation, 2200 Mission College Blvd. Santa Clara, CA 95054-1549 USA) at 2.40 GHz for a total of 224 cores with InfiniBand connection.

7. FFOWCS WILLIAMS AND HAWKINGS FORMULATION COUPLING

Because in the far-field the mean flow is essentially uniform, it is possible to switch in this part of the domain to a less computationally demanding mathematical model such as the wave equation to reduce the computational effort. This can be done by coupling the DGM with the three-dimensional integral formulation of the wave equation proposed by Ffowcs Williams and Hawkings [17]. Knowing the acoustic field on a control surface, it is possible to calculate the acoustic pressure at very long distances evaluating only two integrals over the surface itself, and the computational cost does not depend upon the position of the listener. Far-field directivities can be computed very efficiently.

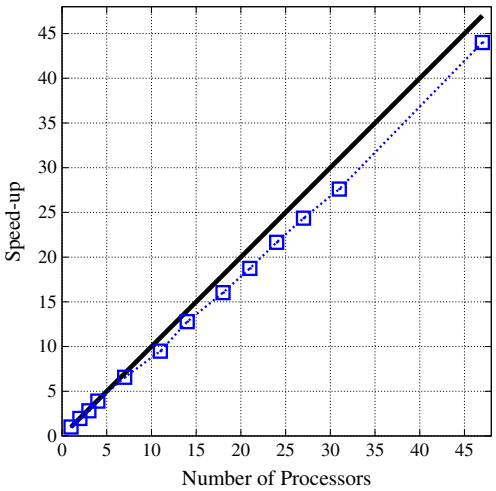

Figure 5. Scalability of the DGM. (—) Linear scaling, (· · ·) numerical speed up.

The control surface must be located in a region where the mean flow field is almost uniform and the LEE or APE solution is known. In this way it is ensured that the control surface, treated as a permeable closed surface, contains in its interior all the noise sources. For a uniform mean flow of Mach number M and aligned with the z axis, the FW-H integral can be written, in the frequency domain, for a Cartesian coordinate system as [33, 34]

$$H\left(f\right)c_0 2\hat{\rho}\left(\mathbf{y},\omega\right) = -\int_{\sigma} \mathrm{I}\omega\hat{Q}\left(\boldsymbol{\xi},\omega\right)G\left(\mathbf{y};\boldsymbol{\xi}\right)\,\mathrm{d}\sigma - \int_{\sigma} \hat{F}_i\left(\boldsymbol{\xi},\omega\right)\frac{\partial G\left(\mathbf{y};\boldsymbol{\xi}\right)}{\partial y_i}\,\mathrm{d}\sigma\,, \tag{34}$$

where σ defines the integration surface, $\boldsymbol{\xi}$ are the surface coordinates and $\mathbf{y}$ are the listener coordinates. Moreover, considering that the present FW-H formulation will be applied only to problems where there is no noise contribution because of turbulence, the quadrupole term in Equation (34) is omitted.

The Green's function G is defined as

$$G = -\frac{1}{4\pi R\beta}\mathrm{e}^{-\mathrm{I}k\left(R/\beta - Mz/\beta^2\right)}\,, \tag{35}$$

with $k = \omega/c_0$, $R = \sqrt{(x-\xi)^2 + (y-\eta)^2 + (z-\zeta)^2/\beta^2}$, $M = w_0/c_0$ and $\beta = \sqrt{1-M^2}$. The source terms $\hat{Q}$ and $\hat{F}_i$ are obtained by evaluating the functions Q and F_i defined in the time domain as

$$F_i = \left[\delta_{ij}\left(p_0 + p'\right) + \left(\rho_0 + \rho'\right)\left(u_i' - w_0\delta_{3i}\right)\left(u_j' + w_0\delta_{3j}\right) + \rho_0 w_0 2\delta_{3i}\delta_{3j}\right]\hat{n}_j\,, \tag{36}$$

$$Q = \left[\left(\rho_0 + \rho'\right)\left(u_i' + w_0\delta_{3i}\right) - \rho_0 w_0\delta_{3i}\right]\hat{n}_i\,, \tag{37}$$

and then applying the Fourier transform. $\hat{n}_i$ is the outward directed unit normal vector to the surface σ. A prime denotes the acoustic perturbations from free stream conditions $(.)_0$. The quantities necessary to compute Q and F_i are extracted from the acoustic field solved with the DGM. When dealing with axisymmetric problems, near-field calculations are performed only in the (x, z) plane; however, because the FW-H model is fully three-dimensional, the acoustic field must be reconstructed over the whole three-dimensional integration surface. The points of the integration surface on the plane $\theta = 0$, with $y/x = \tan\theta$, are localized inside the near-field mesh and then the corresponding acoustic values are interpolated from the nodal values of the element containing the surface point. The acoustic values are then extended on the whole three-dimensional integration surface using the axisymmetric condition.

8. NUMERICAL RESULTS

To demonstrate the accuracy of the method, several numerical tests have been performed. For all the reported test cases, if not explicitly indicated, the variables are made nondimensional by the reference mean-flow values, that is, c_0, ρ_0, p_0 and by a reference length, chosen accordingly to the considered case. Moreover, the mean flow is computed analytically in the initialization step.

8.1. Multigeometry scattering problem

The scattering of sound generated by a spatially distributed monopole source from three rigid circular cylinders is considered, as defined in the Fourth Computational Aeroacoustics (CAA) Workshop on Benchmark Problems [35]. This case provides a severe test of the ability of the DGM to resolve complex geometries. The acoustic-scattering problem is governed by the LEE, where the time-dependent acoustic-source term on the right-hand side is different from zero only for the energy equation. In this case, LEE and APE coincide because no mean flow is present. The forcing term S_{energy} is a Gaussian function and can be written in a source-centered coordinate system as

$$S_{\text{energy}} = \epsilon\exp\left[-\ln(2)\cdot\left(\frac{x_S^2 + y_S^2}{b^2}\right)\right]\sin\left(\omega t\right), \tag{38}$$

where $\epsilon = 1$, $\omega = 8\pi$ and $b = 0.2$. The cylinders have unequal diameters ($D_1 = 1.0$, $D_2 = 0.75$, $D_3 = 0.75$), with the source located on the x-axis in $(0, 0)$. In the (x_S, y_S)-coordinate system centered on the source, the locations of the cylinders are given by $L_1 = (-3, 0)$, $L_2 = (3, 4)$ and $L_3 = (3, -4)$. Considering the symmetry of the problem, only the $y \geqslant 0$ half-domain can be considered, treating the x-axis as an acoustically rigid wall. The physical domain extends for $x \in [-8, 8]$, $y \in [0, 7.5]$ and is surrounded by a PML region with a thickness equal to 1.5. This domain is discretized with approximately $50,000$ elements (Figure 6(a)). To optimize the computational time, the variable interpolation order approach is used. The distribution of the degree of elements can be seen in Figure 6(b). On the x-axis and on the surface of the cylinders the mesh is refined and the lowest order $p = 3$ is used. Moving towards the far-field boundaries the mesh becomes coarser and the polynomial degree increases up to $p = 7$, following distribution in Equation (33). In this test case, the grid and the monopole frequency considered give $\alpha_d \approx 25$ in Equation (33).

Figure 7 shows the isocontours of the computed mean-square fluctuating-pressure field over the entire resolved portion of the computational domain, including the PML. In Figures 8 and 9, the RMS of the fluctuating pressure is plotted along the center line and on the surface of the cylinders. Figure 9 shows a very good agreement between the numerical and the analytical solution [35].

8.2. Sound propagation around a high-lift airfoil

The scattering of a monopole source, in a medium at rest, from a high-lift airfoil geometry is considered here to assess the efficiency of the variable-element degree approach. Also in this case,

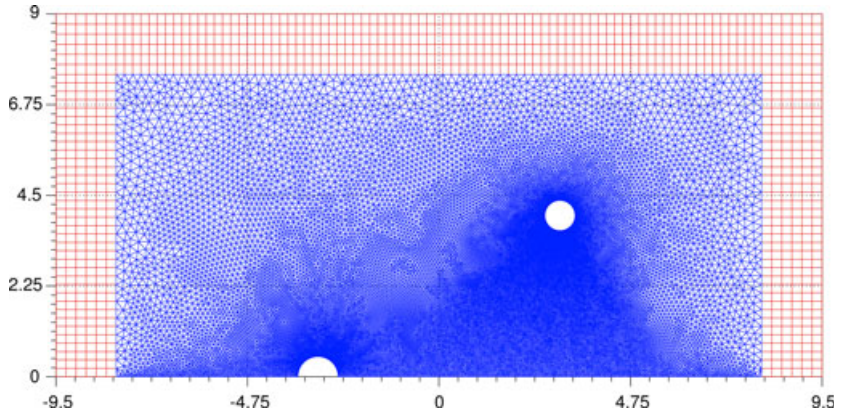

(a)

(b)

Figure 6. Multigeometry scattering problem: (a) mesh of internal and PML domains and (b) element degree distribution.

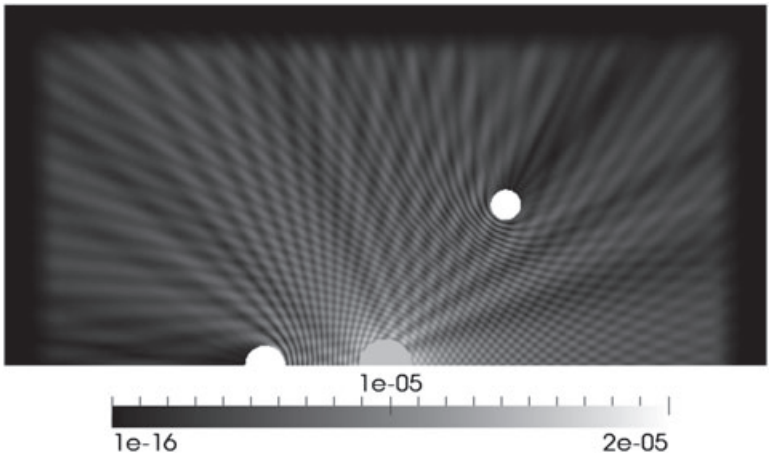

Figure 7. Root-mean-square (RMS) of the fluctuating pressure field.

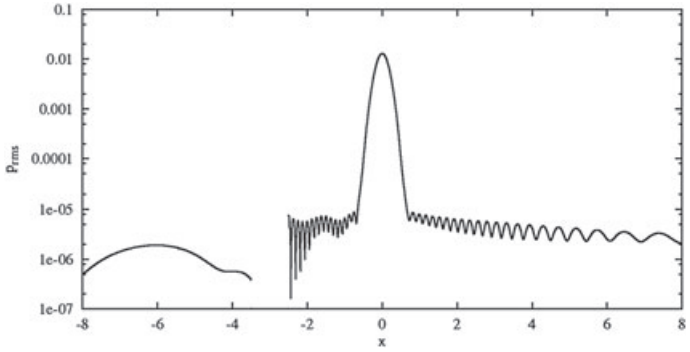

Figure 8. RMS of the fluctuating pressure along the x axis.

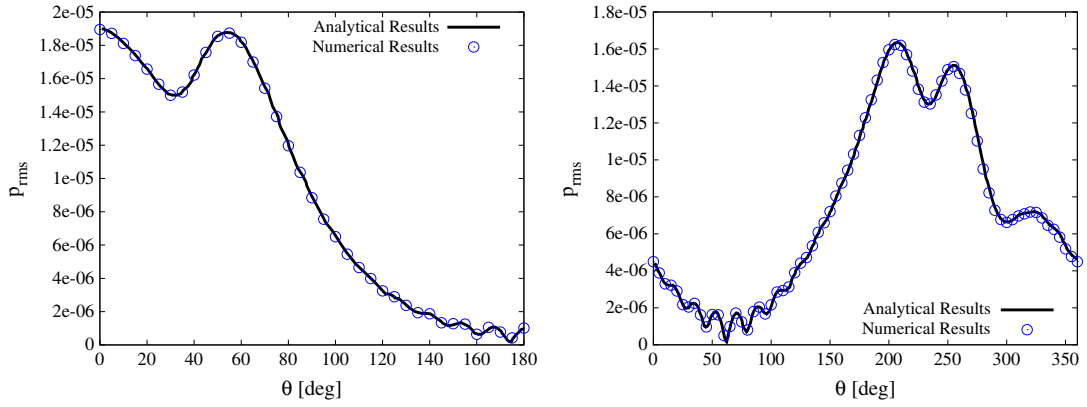

Figure 9. RMS of the fluctuating pressure on the surface of the cylinders: (∘) numerical, (—) analytical; (a) left cylinder and (b) top cylinder.

LEE and APE coincide because no mean flow is present. The geometry is a three-element airfoil based on the RA16SC1 profile, with the slat and flap deflected by 30° and 20°, respectively. The chord in fully retracted configuration is 0.480 m and the computational domain extends for $(x, y) \in [-0.9 \text{ m}; 0.9 \text{ m}]$ and it is surrounded by vertical and horizontal PML layers with a thickness of 0.1 m. The domain is discretized using an unstructured grid with about 6700 elements, as

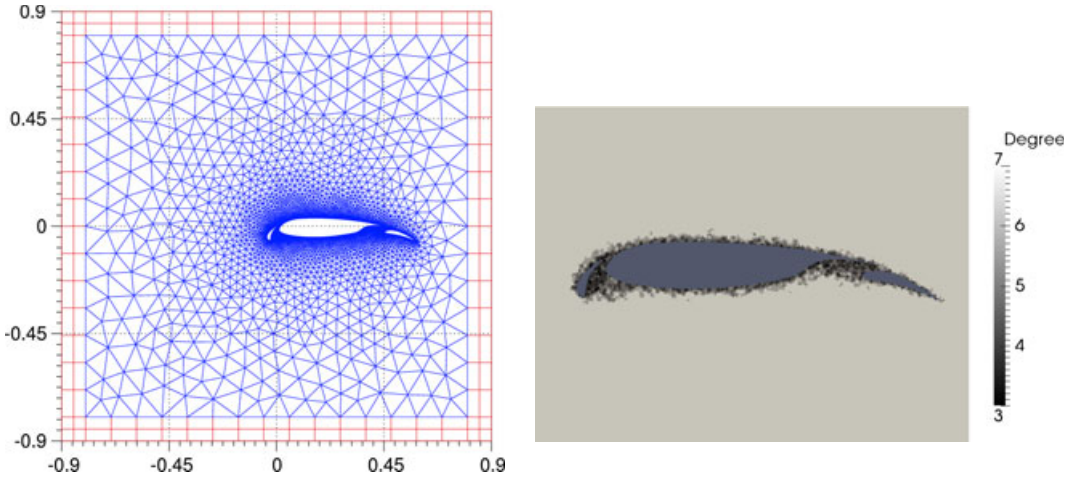

(a) (b)

Figure 10. High-lift airfoil case: (a) mesh of internal and PML domains and (b) element degree distribution.

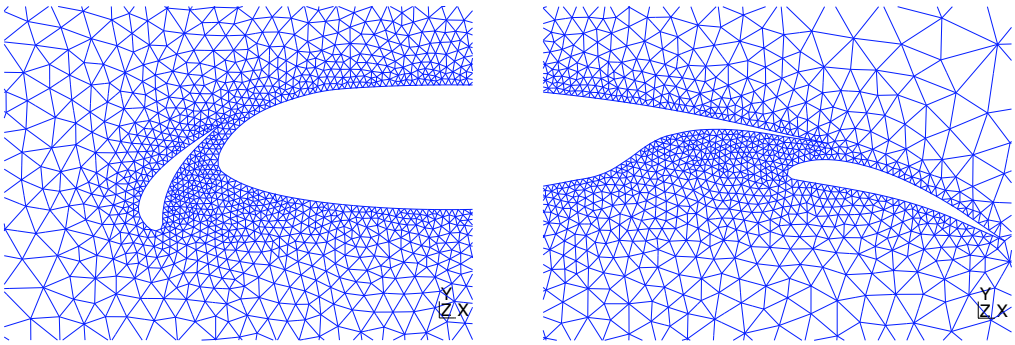

(a) (b)

Figure 11. Mesh refinement of the (a) slat and (b) flap.

shown in Figure 10(a). The grid is refined in proximity of the slat and of the flap (see Figures 11(a) and (b)), whereas it is coarse in the outer region where there is free space propagation.

The only acoustic source is a monopole placed near the trailing edge of the slat, forcing the energy equation as

$$S_{\text{energy}} = \epsilon \exp\left[-\ln(2) \cdot \left(\frac{x_S^2 + y_S^2}{b^2}\right)\right] \sin(\omega t) \ , \tag{39}$$

with $\omega = 2\pi f$, $f = 5000$ Hz, $\epsilon = 1$ Pa, $b = 0.01$ m and $(x_S, y_S) = (0.02\ \text{m}, 0.02\ \text{m})$. Different computations are performed with a constant element degree, from $p = 3$ to $p = 7$ and with the variable element degree approach. In the latter case the element degree is relaxed in proximity of the airfoil from $p = 7$ to $p = 3$ following Equation (33), with $\alpha_d \approx 43$. The distribution of the element degree is shown in Figure 10(b). The solution obtained with a constant element degree of $p = 7$ is taken as reference solution. Figure 12 shows the pressure distribution for the reference solution when a periodic regime is reached.

To compare the solutions obtained using constant and variable element degree, the RMS of the acoustic pressure distribution is extracted on a circle centered in $(0, 0)$ with a radius of 0.7 m. From Figure 13 it is evident that the variable order solution is in excellent agreement with the reference one, whereas the other cases suffer from the error because of under-resolution in the coarse region.

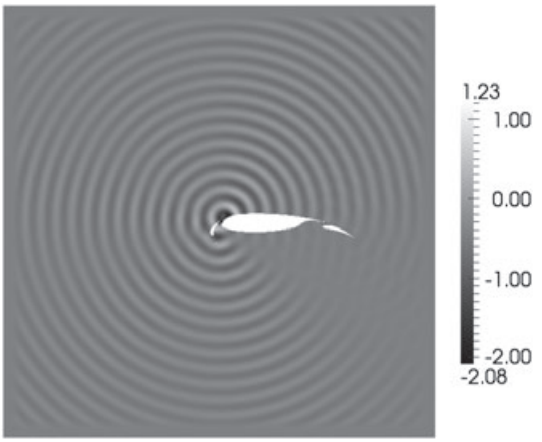

Figure 12. Instantaneous pressure field after 30 periods, Pa.

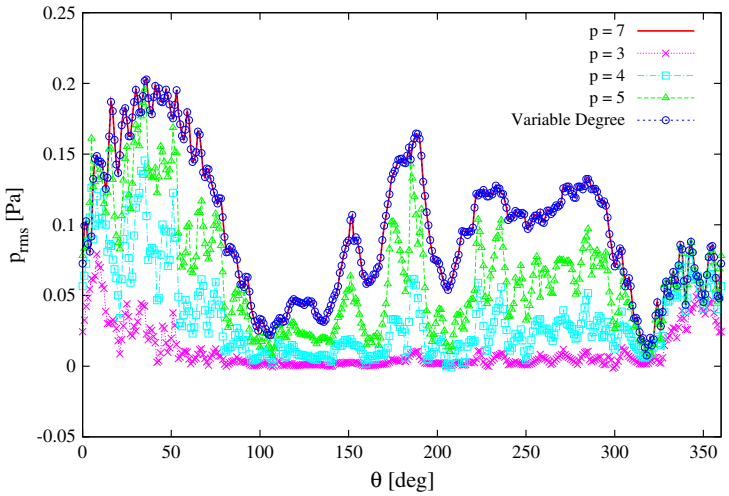

Figure 13. Directivity of acoustic pressure RMS at 0.7 m. Comparison of constant and variable element degree.

The advantage of using a variable element degree approach is noticeable comparing both the error with respect to the reference solution and the computational time (see Table I). With the variable element degree distribution the simulation is three times faster than the reference solution and the error is limited to $4.12 \cdot 10^{-4}$. Whereas a constant distribution with $p = 6$ is only 1.35 times faster than the reference solution but has an L_1-error of $1.17 \cdot 10^{-2}$.

8.3. Munt and extended Munt problems

To further validate the numerical model and to verify the effectiveness of the coupling with the FW-H formulation, the acoustic diffraction of a plane wave propagating out of a semi-infinite cylindrical duct is studied. The duct wall has no thickness with acoustically rigid inner and outer surfaces. Two configurations are studied: in the first one, termed 'Munt problem', the geometry consists of a single cylindrical duct, whereas in the second one, termed 'Extended Munt problem', inside the duct there is a rigid infinite hub. The two configurations are depicted in Figures 14(a) and (b). For the 'Munt problem' the analytical solution has been found in [36] and it has been subsequently generalized for annular ducts and lined walls [37–39]. Results for these test cases are presented in dimensional variables. In both cases presented here LEEs are used.

Table I. L_1 norm of error and normalized computational time with respect to the reference solution (constant element degree of $p = 7$). The evaluation of the error is achieved on the RMS of the acoustic pressure extracted on a circle centered in $(0, 0)$ with a radius of 0.7 m.

	L_1 (Error)	Normalized time
Constant element degree		
$p = 3$	$8.72 \cdot 10^{-2}$	0.10
$p = 4$	$6.43 \cdot 10^{-2}$	0.29
$p = 5$	$3.46 \cdot 10^{-2}$	0.54
$p = 6$	$1.17 \cdot 10^{-2}$	0.74
$p = 7$	-	1
Variable ($p = 3 \rightarrow p = 7$)	$4.12 \cdot 10^{-4}$	0.34

For the 'Munt Problem' the mean flow is assumed to be at rest both inside and outside of the duct, with a speed of sound equal to $c_0 = 340.17$ m/s and a density equal to $\rho_0 = 1.225$ kg/m^3. Because the analytical solution is available only for points at great distance from the cylinder exit, it is not possible to compare directly the solution of LEE obtained using the DGM with the analytical one. Instead, LEEs are solved only in a small computational domain, the near-field domain, and then the far-field solution is evaluated from the near-field one using the Ffowcs Williams and Hawkings equation. The far-field results are then compared with the analytical solution.

Assuming a duct radius of $r_1 = 1.212$ m, the near-field computational domain extends for $z \in [-2.5 \text{ m}; 5.5 \text{ m}]$ and for $r \in [0.0 \text{ m}; 3.9 \text{ m}]$, and is surrounded by vertical and horizontal PML layers with a thickness of 0.5 m. This domain is discretized using a uniform structured grid with about 35,000 triangular elements and the computation is performed using Lagrangian polynomials of degree $p = 3$. For the far-field computation the integration surface is a cylinder with radius 1.24 m closed in the fore region by a semisphere centered at the duct exit plane. The surface is discretized with a grid, uniform in both z and θ directions. The number of points per wavelength on the integration surface is chosen to be larger than the corresponding value for the near-field acoustic mesh.

(a) (b)

Figure 14. (a) Munt problem geometry and (b) extended Munt problem geometry.

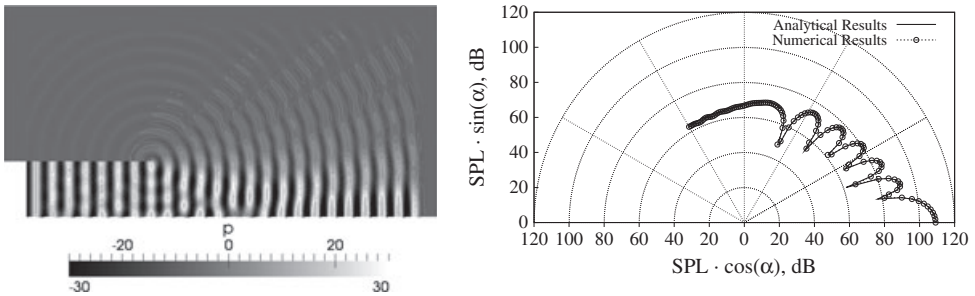

(a) (b)

Figure 15. Munt problem: plane wave $f = 956$ Hz, $M_1 = M_2 = 0$; (a) near-field pressure distribution, Pa; (b) far-field Sound-Pressure-Level (SPL) directivity at $r = 46$ m.

A plane wave with unitary incident intensity and frequency equal to 956 Hz is studied. In Figure 15(a) the near-field instantaneous pressure field is shown, whereas in Figure 15(b) the corresponding far-field SPL directivity pattern is presented. The directivity is evaluated on an arc having the center defined at the center of the duct exit section and radius equal to $r = 46$ m. The agreement between the numerical and the analytical solution is very good.

For the 'Extended Munt Problem', there is a mean flow velocity inside the duct, with Mach number equal to 0.447, whereas the fluid outside the duct is at rest. There is no shear layer between the two flows, instead they are separated by a vortex sheet. Assuming a duct radius $r_1 = 1.212$ m and a hub radius $r_2 = 0.947$ m, the computational domain extends for $z \in [-2.5\text{ m}; 6.5\text{ m}]$ and for $r \in [0.0\text{ m}; 5.8\text{ m}]$, and it is surrounded by vertical and horizontal PML layers with a thickness of 0.5 m. This domain is discretized using a uniform structured grid with about 5000 quadrangular elements and the computation is performed using Lagrangian polynomials of degree $p = 6$.

The incoming wave is planar varying harmonically in time with frequency 866 Hz and its amplitude is such that the incident intensity is unitary. In Figure 16(a), the instantaneous pressure distribution is reported, whereas Figure 16(b) shows the comparison of the computed SPL with the analytical solution [39]. The directivity in the near field is evaluated on an arc having the center defined at the center of the duct exit section and radius equal to $r = 4.848$ m. The agreement with the analytical results is good, with a correct representation of the lobes in the directivity pattern, except for a small discrepancy at $\theta \approx 40°$, because in the numerical computation the Kutta condition is not explicitly imposed as in the analytical solution.

8.4. Kelvin–Helmholtz instability

The problem considers the propagation of the sound generated by a monopole placed in a bounded mean shear flow aligned with the x axis. The mean flow is analytically provided. In this case the LEE and APE solutions differ. The APE solution does not give rise to Kelvin–Helmholtz instability as in the case of the solution of the LEE.

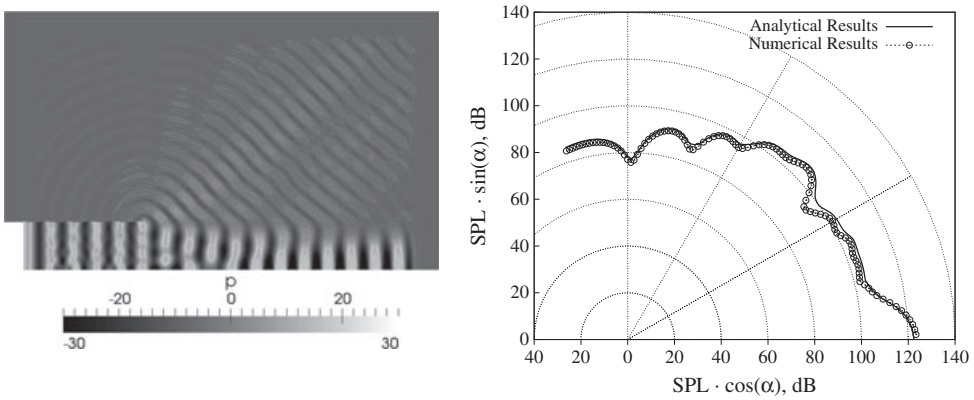

(a) (b)

Figure 16. Extended munt problem: plane wave $f = 866$ Hz , $M_1 = 0.447$, $M_2 = 0$; (a) near-field pressure distribution, Pa; (b) near-field SPL directivity at $r = 4.848$ m.

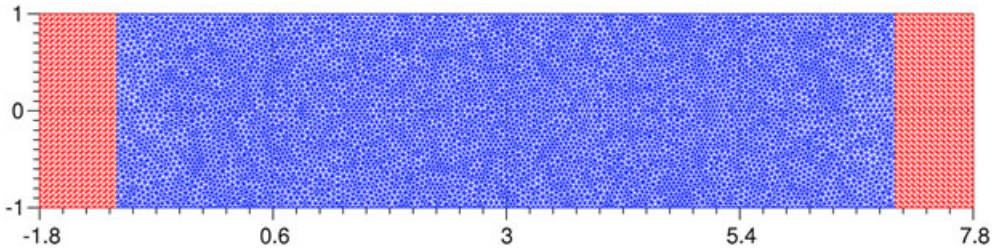

Figure 17. Kelvin–Helmholtz Instability: mesh of the internal and PML domain.

The monopole is placed at the center of a two-dimensional duct with hard walls. The duct extends in the x-direction from -1 to 7 and in the y-direction from -1 to 1. At the two sides of the duct, PML layers of thickness 0.8 are added, enabling the acoustic waves to leave without spurious reflections. The computational domain is discretized with about 15, 000 elements (Figure 17) and polynomials of constant order $p = 3$ are used.

The mean velocity profile of the mixing layer is given by the expression

$$u_0(y) = \frac{1}{2}\left[(U_1 + U_2) + (U_1 - U_2)\tanh\left(\frac{2y}{\delta}\right)\right], \tag{40}$$

and the mean density profile is

$$\rho_0(y) = \frac{1}{T_0(y)}\,. \tag{41}$$

The mean temperature $T_0(y)$ is determined by the Crocco relation for compressible flows with $\gamma = 1.4$, and reads

$$T_0(y) = T_1\frac{u_0 - U_2}{U_1 - U_2} + T_2\frac{U_1 - u_0}{U_1 - U_2} + \frac{\gamma - 1}{2}(U_1 - u_0)(u_0 - U_2)\,. \tag{42}$$

The flow parameters are [16]:

$$U_1 = 0.8, \quad U_2 = 0.2, \quad \delta = 0.4, \quad T_1 = 1, \quad T_2 = 0.8\,. \tag{43}$$

Mean velocity along the x axis and density profiles in y direction are reported in Figure (18). Adding the following monopole source term to the energy equation

$$S_{\text{energy}} = \sin(1.5t)e^{-\ln(2)(x^2+y^2)/0.05^2}\,, \tag{44}$$

it follows that the forcing frequency is of the same order of magnitude of the momentum thickness of the mean shear flow. Under these conditions it can be shown [40] that the vortical mode is excited and hydrodynamic flow oscillations, induced by the associated Kelvin–Helmholtz instability, occur. Figures 19(a) and (b) show the instantaneous LEE and APE solutions at $t = 16$, respectively. It is noticeable that in the LEE solution the oscillating vortical mode is overwhelming the acoustical mode, which can hardly be identified. On the contrary, in the APE solution vorticity modes are not present and the acoustic field of a monopole in a duct is fully recognizable.

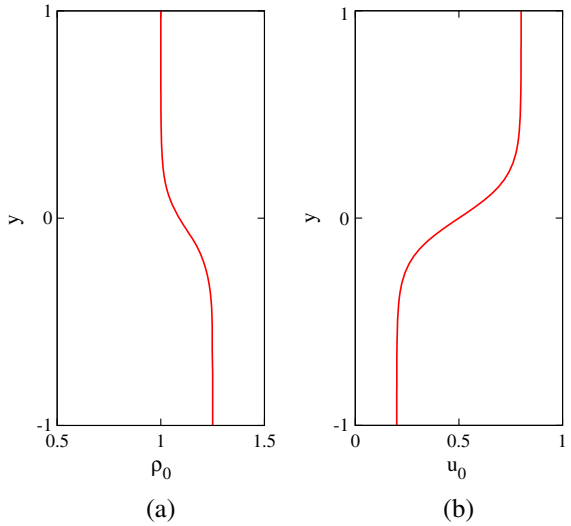

Figure 18. (a) Mean velocity along the x axis and (b) density profile.

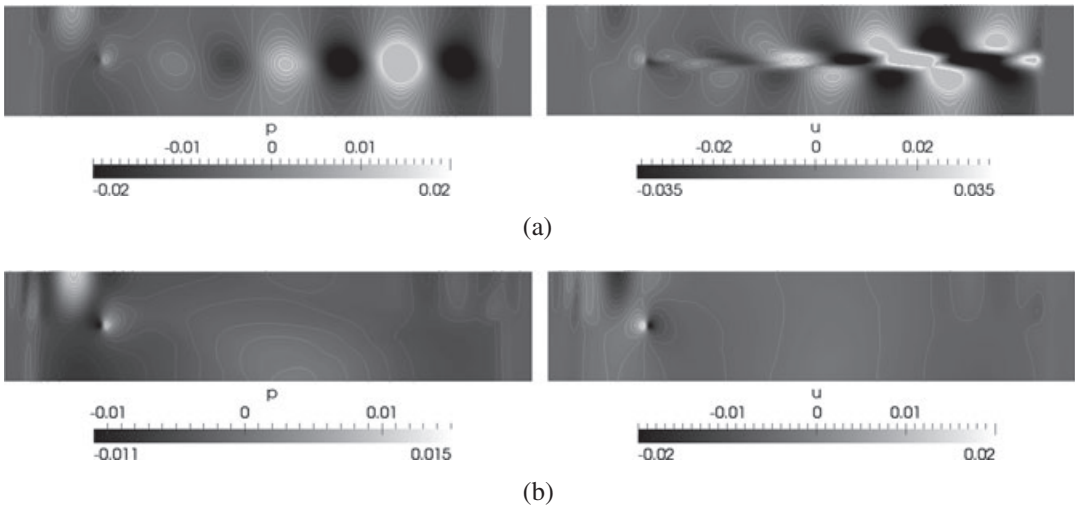

Figure 19. Instantaneous pressure and x component velocity fields at $t = 16$: (a) Linearized Euler equations and (b) acoustic perturbation equations.

9. CONCLUSIONS

A high-order, parallel DGM with a PML nonreflecting boundary condition treatment has been presented. The DGM has been applied to both the LEE and the APE for the numerical simulation of aeroacoustic propagation in two-dimensional and axisymmetric problems, with triangular and quadrilateral elements. To improve computational efficiency and accuracy a new strategy of variable interpolation order is proposed. Moreover, the DGM has been implemented with the quadrature-free approach and computations are parallelized. In addition, a new wall boundary condition, based on the solution of the Riemann problem, is proposed. It is shown that it is more accurate than extrapolating the wall values from neighbor cells, with no additional computational cost. The time discretization is based on a low dissipation formulation of a fourth-order accurate Runge–Kutta scheme. Coupling the DGM with the three-dimensional FW-H integral formulation of the wave equation, it has been possible to efficiently evaluate far-field directivity patterns.

Accuracy tests have proven that, using a Lagrangian basis of degree p, the method converges to the analytical solution with the theoretical rate of $p + 1$. This behavior is conserved also on unstructured grids. Moreover, the parallel implementation achieves a near-linear speed up.

Good agreement with analytical solutions has been shown for a scattering benchmark problem on multiple cylinders, solving the LEE in Cartesian coordinates. The accuracy and efficiency of the variable interpolation order algorithm is assessed for a realistic high-lift airfoil. Comparing the results with the constant order approach the accuracy is retained while reducing sensibly the computational time. The ‘Munt problem’, treating the acoustic diffraction by a plane wave propagating out of a semi-infinite cylindrical duct, with and without a uniform mean flow inside the duct, has been computed solving the LEE in axisymmetric coordinates. The numerical far-field directivities, obtained with the FW-H formulation, were successfully compared with the analytical solutions.

As a last case, the acoustic propagation inside a two-dimensional duct with a nonuniform mean flow has been studied. Both the LEE and APE equations are solved, showing that the DGM is able to correctly reproduce the hydrodynamic instabilities in the case of the LEE, and to resolve the acoustic field in the case of the APE.

All the numerical results show that the implemented DGM is accurate and efficient, and therefore well-suited for solving large-scale aeroacoustic problems in complex geometries. Further investigations will extend the present DGM to three-dimensional problems.

REFERENCES

1. Tam CKW, Webb JC. Dispersion-Relation-Preserving finite difference schemes for computational acoustics. *Journal of Computational Physics* 1993; **107**:262–281.
2. Reed WH, Hill TR. Triangular mesh methods for the neutron transport equation. *Technical Report LA-UR-73-479*, Los Alamos Scientific Laboratory, 1973.
3. Bassi F, Rebay S. A high-order accurate discontinuous finite element method for the numerical solution of the compressible Navier-Stokes equations. *Journal of computational physics* 1997; **131**:267–279.
4. Cockburn B, Karniadakis G, Shu C-W. *Discontinuous Galerkin methods. Theory, computation and applications*. Springer-Verlag, 2000.
5. Hu FQ, Atkins HL. Eigensolution analysis of discontinuous Galerkin method, Part I. *Journal of Computational Physics* 2002; **182**:516–545.
6. Hu FQ, Atkins HL. Two-dimensional wave analysis of the discontinuous Galerkin method with non-uniform grids and boundary conditions. *8th AIAA/CEAS Aeroacoustics Conference; Breckenridge, CO; AIAA Paper*, 2002; 2002–2514.
7. Ainsworth M. Dispersive and dissipative behaviour of high order discontinuous Galerkin finite element method. *Journal of Computational Physics* 2004; **198**:106–130.
8. Zhang M, Shu C-W. An analysis of and a comparison between the discontinuous Galerkin and the spectral finite volume methods. *Computers and Fluids* 2005; **34**:581–592.
9. Delorme P, Mazet P, Peyret C, Ventribout Y. Computational aeroacoustics applications based on a discontinuous Galerkin method. *Comptes Rendus Mécanique* 2005; **333**:676–682.
10. Bernacki M, Fezoui L, Lanteri S, Piperno S. Parallel discontinuous Galerkin unstructured mesh solvers for the calculation of three-dimensional wave propagation problems. *Applied Mathematical Modelling* 2006; **30**:744–763.
11. Landmann B, Kessler M, Wagner S, Krämer E. A parallel, high-order discontinuous Galerkin code for laminar and turbulent flows. *Computer and Fluids* 2008; **37**:427–438.
12. Atkins HL, Shu C-W. Quadrature-free implementation of the discontinuous Galerkin method for hyperbolic equations. *AIAA Journal* 1998; **36**(5):775–782.
13. Ewert R, Schröder W. Acoustic perturbation equations based on flow decomposition via source filtering. *Journal of Computational Physics* 2003; **188**(2):365–398.
14. Chevaugeon N, Hillewaert K, Gallez X, Ploumhans P, Remacle J-F. Optimal numerical parameterization of discontinuous Galerkin method applied to wave propagation problems. *Journal of Computational Physics* 2007; **223**:188–207.
15. Berland J, Bogey C, Bailly C. Low-dissipation and low-dispersion fourth-order Runge-Kutta algorithm. *Journal of computational physics* 2006; **35**:1459–1463.
16. Hu FQ. A perfectly matched layer absorbing boundary condition for LEE with a non-uniform mean flow. *Journal of Computational Physics* 2005; **208**:469–492.
17. Williams JEF, Hawkings DL. Sound generation by turbulence and surfaces in arbitrary motion. *Proceedings of the royal society* 1969; **264**:321–342.
18. Hesthaven JS. From electrostatics to almost optimal nodal sets for polynomial interpolation in a simplex. *SIAM Journal on Numerical Analysis* 1998; **35**:655–676.
19. Schmidt W, Jameson A, Turkel E. Numerical solution of the Euler equations by finite volume methods using Runge-Kutta time stepping schemes. *AIAA Paper* 1981:81–1259.
20. Hu FQ, Hussaini MY, Manthey JL. Low-dissipation and low-dispersion Runge-Kutta schemes for computational acoustics. *Journal of Computational Physics* 1996; **124**:91–177.
21. Williamson JH. Low-storage Runge-Kutta schemes. *Journal of computational physics* 1980; **35**:48–56.
22. Goldstein M. *Aeroacoustics*. McGraw-Hill, 1976.
23. van der Vegt JJW, vander Ven H. Slip flow boundary conditions in discontinuous Galerkin discretizations of the Euler equations of gas dynamics. In *proceedings fifth world congress on computational mechanics*, H.A. Mang, F. Rammerstorfer, J. Eberhardsteiner (eds), 2002; 1–16.
24. Thompson KW. Time-dependent boundary conditions for hyperbolic systems II. *Journal of Computational Physics* 1990; **89**:439–461.
25. Giles MB. Non-reflecing boundary conditions for Euler equation calculations. *AIAA Journal* 1990; **28**(12):2050–2058.
26. Bodony DJ. Analysis of sponge zones for computational fluid mechanics. *Journal of Computational Physics* 2006; **212**:681–702.
27. Hu FQ. On absorbing boundary conditions of linearized Euler equations by a perfectly matched layer. *Journal of Computational Physics* 1996; **129**:201–219.
28. Tam CKW, Auriault L, Cambulli F. Perfectly matched layers as an absorbing boundary condition for the linearized Euler equations in open and ducted domains. *Journal of Computational Physics* 1998; **144**:213–234.
29. Hu FQ. A stable, perfectly matched layer for linearized Euler equations in unsplit physical variables. *Journal of Computational Physics* 2001; **173**:455–480.
30. Özyörük Y. Numerical prediction of aft radiation of turbofan tones through exhaust jets. *Journal of Sound and Vibration* 2009; **325**(1–2):122–144.
31. Toulorge T, Desmet W. Curved boundary treatments for the discontinuous Galerkin method applied to aeroacoustic propagation. *AIAA Journal* 2010; **48**(2):479–489.

32. Karypis G, Kumar V. A fast and highly quality multilevel scheme for partitioning irregular graphs. *SIAM Journal on Scientific Computing* 1999; **20**(1):359–392.
33. Lockard DP. An efficient, two-dimensional implementation of the Ffowcs Williams and Hawkings equation. *Journal of Sound and Vibration* 2000; **229**(4):897–911.
34. Iob A, Arina R, Schipani C. A frequency-domain linearized Euler model for turbomachinery noise radiation through engine exhaust. *AIAA Journal* 2010; **48**(4):848–858.
35. Sherer SE. Acoustic scattering from multiple circular cylinders: Category 2, problems 1 and 2, analytic solution. *Proceedings of the 4th CAA workshop on benchmark problems, NASA CP-2004-212954*, 2004.
36. Munt RM. The interaction of sound with a subsonic jet issuing from a semi-infinite cylindrical pipe. *Journal of Fluid Mechanics* 1977; **83**(4):609–640.
37. Rienstra SW. Acoustic radiation form a semi-infinte annular duct in a uniform subsonic mean flow. *Journal of Sound and Vibration* 1984; **94**(2):267–288.
38. Gabard G, Astley RJ. Theoretical model for sound radiation from annular jet pipes: Far- and near-field solutions. *Journal of Fluid Mechanichs* 2006; **549**:315–341.
39. Demir A, Rienstra S. Sound radiation from an annular duct with jet flow and a lined centerbody. *12th AIAA/CEAS Aeroacoustics Conference; Cambridge, Ma; AIAA Paper 2006-2718*, 2006.
40. Manera J, Schiltz B, Leneveu R, Caro S, Jacqmot J, Rienstra S. Kelvin-Helmholtz instabilities occurring at a nacelle exhaust. *14th AIAA/CEAS Aeroacoustics Conference; Vancouver, Canada; AIAA Paper 2008-2883*, 2008.